Range–Doppler Analysis for Rain Detection at Ka-Band: Numerical and Experimental Results From Laboratory and Field Measurements

Ashkan Taremi Zadeh, Moritz Mälzer, Jonas Simon, Sebastian Beck, Jochen Moll, and Viktor Krozer, *Senior Member, IEEE*

***Abstract*—Radar technology in the millimeter-wave frequency band offers many interesting features for wind park surveillance, such as structural monitoring of rotor blades or the detection of bats and birds in the vicinity of wind turbines (WTs). Currently, the majority of WTs are affected by shutdown algorithms to minimize animal fatalities via direct collision with the rotor blades or barotrauma effects. The presence of rain is an important parameter in the definition of those algorithms together with wind speed, temperature, time of the day, and season of the year. A Ka-band frequency-modulated continuous-wave radar (33.4–36.0 GHz) installed at the tower of a 2-MW WT was used during a field study. We have observed characteristic rain-induced patterns, based on the range–Doppler algorithm. To better understand those signatures, we have developed a laboratory experiment and implemented a numerical modeling framework. Experimental and numerical results for rain detection and classification are presented and discussed here. Based on this article, a bat- and bird-friendly adaptive WT control can be developed for improved WT efficiency in periods of rain and, at the same time, reduced animal mortality.**

***Index Terms*—Atmosphere, millimeter wave radar, radar signal processing, wind energy.**

I. Introduction

THE expansion of wind energy worldwide is characterized by a dynamic development [1]. This leads, on one hand, to an increased amount of electrical energy generated from renewable resources. On the other hand, high mortality of bats and birds was recorded [2], [3], primarily due to a direct collision of the animals with the rotor blades or through barotrauma effects [4]. Bats are a threatened species in European countries, such as Germany, particularly for migratory bats that pass wind turbines (WTs) during their migration flights [5]. European bats are highly vulnerable as predators of insects, and that is why, protecting these animals is critically important for a working ecosystem and public acceptance of wind energy development.

Moreover, the German government forced WT operators to implement shutdown algorithms for a majority of WTs in Germany, to reduce bat and bird fatalities to a minimum. The main features of those algorithms are environmental factors, such as wind speed and temperature, combined with time of the day and season of the year [6]. More recently, rain has become an important additional parameter of shutdown algorithms so that WTs can operate in the presence of rain for increased WT rentability [7]. The underlying argument is related to the flight behavior of bats. For example, the authors in [8] discovered that wet bats must spend twice as much energy as dry ones to stay aloft. While dry bats burn ten times more energy during flight than they do at rest, wet bats burn 20 times more energy. In addition, insects hide in rain making the hunting of insects less attractive. Moreover, the bat echolocation calls are negatively affected by strong atmospheric attenuation in the ultrasound frequency range when the humidity is high [9], [10]. Therefore, it is valuable to have real-time information about rain and its intensity in the relevant airspace close to a WT during day and night (see Fig. 1). We address this problem by numerical modeling of rainfall and dedicated experimental measurements in the laboratory. Moreover, results from a 2-MW turbine with concurrent camera recordings for validation will be presented. The benefit of this article would be an adaptable WT control during periods of rain for an improved WT efficiency. An additional benefit is, on one hand, local weather forecast information with very high resolution and additional parameters for

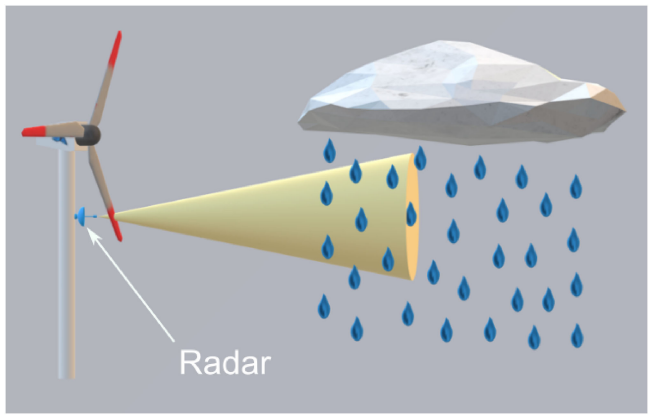

Fig. 1. Illustration of radar-based rain detection in the relevant flight zone of bats and birds.

Manuscript received October 15, 2019; revised January 21, 2020; accepted February 9, 2020. Date of publication March 5, 2020; date of current version March 20, 2020. This work was supported by the Federal Ministry for Economic Affairs and Energy under Grant 0324323C. *(Corresponding author: Ashkan Taremi Zadeh.)*

The authors are with the Department of Physics, Goethe University Frankfurt, 60438 Frankfurt, Germany (e-mail: taremizadeh@physik.uni-frankfurt.de; maelzer@physik.uni-frankfurt.de; jonas.simon@gmx.net; beck.seb@gmx.de; moll@physik.uni-frankfurt.de; Krozer@physik.uni-frankfurt.de).

Digital Object Identifier 10.1109/JSTARS.2020.2975281

behavioral models describing the flight routes of migrating bats and birds.

II. Related Work: Weather Radars

The work presented here is strongly related to weather radars. Hence, the following section reviews the state-of-the-art: The basic operation principle is the same for all the weather radar devices. Differences normally exist in the variation of parameters that can be optimized for a particular expected outcome. Especially, the operating frequency band is of high importance, because its choice determines the attenuation of the electromagnetic waves by the atmosphere. Also, the working frequency determines the possible penetration depth into the precipitation areas and which objects from this area contribute to a reflection. Some of these radars are capable of operating in the frequency-modulated continuous-wave (FMCW) mode, which provides high-range resolution of clouds and hydrometeors [11].

Doppler weather radars in X- and S-bands are widely used. These radar systems are coherent on the receiving path and can measure Doppler frequencies. In addition to the spatial distribution of the rain intensity, the radial velocity of the rain is determined on the basis of the Doppler effect. Small-scale changes in the radial velocity can be indicators of air circulations [12]. A variant is polarimetric Doppler radars that exploit different polarizations for additional information about the shape and the type of precipitation [13].

Furthermore, radar systems operating at 35 GHz (Ka-band) have been used for rain detection and the estimation of rain intensity. Chandra *et al.* [14] used a vertically pointing 35-GHz Doppler radar. The so-called A–R relation was applied for rain rate estimation at high Doppler velocities ($v > 5$ m/s), whereas the Z_e–R relationship was used for lower Doppler velocities ($v < 5$ m/s). A related system was introduced in [15], where the authors were able to detect echoes from different targets, e.g., cloud droplets, rain, or plankton by estimating the Doppler spectra.

Most of the weather radars mentioned before are not only large, but also costly. This limits their application in wind parks, and especially for installations at single WT, as shown in Fig. 1. In contrast, the proposed millimeter-wave FMCW radar shown later in Fig. 10 is small, lightweight, and of low cost. It combines many sensing tasks besides rain detection, e.g., bat and bird observation, as well as the monitoring of WT blades [16], [17].

III. Theoretical Background

A. Range–Doppler (RD) Analysis

This article is based on the RD algorithm that is widely used in radar applications to determine the position and velocity of moving objects by measuring and processing the Doppler shift in the received signals [18]–[21]. Therefore, an accurate measurement of the reflected frequency is required. The shift between the transmitted frequency and the received frequency determines the object's velocity. An object moving toward the radar leads to a shortening of the wavelength (a positive sign of radial velocity). Conversely, if the object moves away from the radar, this process reverses (a negative sign of radial velocity). According to [22], the relationship between the Doppler frequency f_D and the emitted frequency f_{Tx} is given by

$$f_D = f_{Rx} - f_{Tx} = \frac{2v_r f_{Tx}}{c} \tag{1}$$

where v_r is the velocity of the object toward the radar and c is the speed of light. To form the RD map, the algorithm computes a 2-D fast Fourier transform (FFT) of subsequent radar signals (radargram) to extract the range and Doppler information [23]. Then, we modified the conventional RD algorithm here to eliminate strong static targets and compute the 2-D FFT from the differential radargram representation. The RD map was further processed to prepare a classification of rain intensities at various distances. Therefore, the sum of each column of the RD map $\mathrm{RD}_{ij}(r, v_r)$ was determined as

$$\eta_j(r, v_r) = \sum_{i=1}^{N} \mathrm{RD}_{ij}(r, v_r). \tag{2}$$

In this equation, index i represents the ith range bin and index j the jth bin of the radial velocity v_r.

B. Modeling Rain

Modeling weather conditions can be very valuable to verify the consistency of the radar measurements [24], [25]. Typically, rain follows a Marshall–Palmer raindrop size distribution [26]. This means that the radar cross-section (RCS) is proportional to the diameter of the rain-drop diameter D. In general, for stratiform precipitation, this distribution can be expressed as [26]

$$N_D = N_0 e^{-\Lambda D} \tag{3}$$

with $N_0 = 8000\ \mathrm{m^{-3}mm^{-1}}$, $\Lambda = 4.1R^{-0.21}\ \mathrm{mm^{-1}}$, and R being the rain rate [26]. In this equation, D has the unit mm. Then, to estimate the number of raindrops, as input for the number of point targets in the simulation, we integrated (3), which leads to

$$N = \int_0^\infty N_0 e^{-\Lambda D} dD. \tag{4}$$

Assuming that raindrops are perfect spheres, a maximum reflection from the surface was taken into account for the calculation of the raindrops RCS σ_{RCS}

$$\sigma_{\mathrm{RCS}} = \pi \frac{D^2}{4}. \tag{5}$$

C. Radar Signal Model

The following section describes the radar signal model used for the numerical simulation. Here, the transmitted signal of an FMCW radar can be expressed as

$$s_t(t) = e^{j2\pi(f_c t + \frac{1}{2}\alpha t^2)} \tag{6}$$

where f_c is the carrier frequency, t is the time, and $\alpha = T/B$ is the frequency sweep rate. Like the experimental setup, the sweep time T was chosen as 410 μs and the Bandwidth $B = 2.6$ GHz.

Fig. 2. (Left) Photo of the experimental setup. Water is sprayed from the metal frame toward and away from the radar at different angles. (Right) Rain distribution.

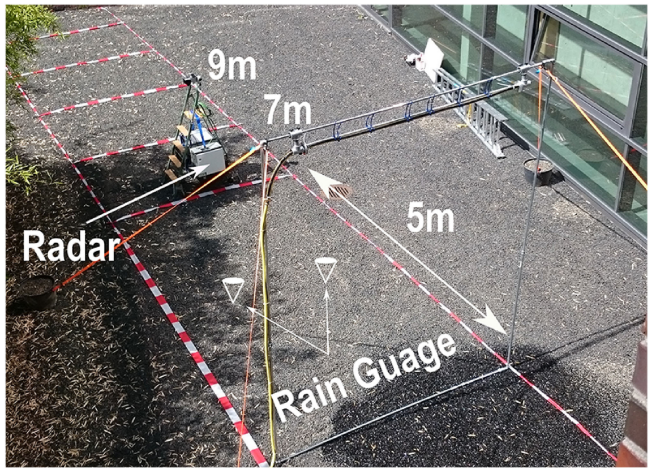

Fig. 3. Bird perspective of the experiment showing different distances of the radar with respect to the metal frame.

The received signal is the delayed and attenuated version of the transmitted signal and can be expressed as [27]

$$s_r(t) = \frac{1}{r^2} e^{j2\pi(f_c(t-\tau)+\frac{1}{2}\alpha(t-\tau)^2)} \tag{7}$$

where τ is the time delay and r is the propagated distance. Then, for generating the intermediate frequency signal, we mix the transmitted and received signals according to [27] as

$$s_{\mathrm{IF}}(t) = \frac{1}{r^2} e^{j2\pi(f_c\tau+\alpha t\tau-\frac{1}{2}\alpha\tau^2)}. \tag{8}$$

For moving targets, the time delay τ is not constant anymore and varies with time. Therefore, assuming a constant radial velocity v_r leads to [27]

$$\tau = \frac{2}{c}(R + v_r t) = \tau_0 + \frac{2}{c} v_r t. \tag{9}$$

Here, τ_0 is the time delay to the stationary target. Then, the RCS is quantitatively calculated in 3-D as

$$\sigma = \lim_{r\to\infty} 4\pi R^2 \frac{|E_s|^2}{|E_i|^2} \tag{10}$$

where E_s and E_i are the far-field scattered and incident electric field intensities, respectively [28].

IV. Laboratory Measurements and Results

A. Description of the Experimental Setup

The laboratory setup, described in the following section, aims at the experimental analysis of rain under controlled conditions. Therefore, we designed a metal frame and placed it vertically in front of the radar, as shown in Figs. 2 and 3. Moreover, a perforated hose is attached to the top metal bar to spray water drops (rain) from different angles (see the left part of Fig. 2). While the angle of rotation θ could be precisely adjusted, the perforation along the hose has an irregular structure, leading to a close to reality distribution, shown in the right part of Fig. 2. Three angles $\theta = -90°$ (toward the radar), $\theta = 90°$ (away from the radar), and $\theta = 0°$ (vertically down) were selected for the experiment. The radar system operates in the FMCW mode in the frequency band from 34.0 to 36.0 GHz. The sweep time was 410 μs during the laboratory and field measurements. This results in approximately 1300 measurements per second that are recorded in the streaming mode using the X3-2M AD converter from Innovation Integration (Camarillo, CA, USA) at a sampling frequency of 5 MS/s. The output power of the radar sensor is about 30 dBm during the field study and 15 dBm during the laboratory experiments. The antenna gain of the horn antennas is approximately 24 dBi [17]. The radar was housed in a weatherproof radome and consisted of one transmitter and two coherent receivers, while the second receiver was only installed for verification purposes (results are the same and not shown in this article). The antennas are horizontally and linearly polarized. The radar was placed at defined distances in front of the metal frame, as depicted in Fig. 3. Two cameras were installed on either side of the radome to validate the radar measurements. During the experiments, the water flow was adjusted and measured by a flow meter so that different rain intensities could be studied. We also used two rain gauges to determine the rain intensity at ground level. In Fig. 4, the values of the content of the rain gauges after each measurement were illustrated.

B. Results

Fig. 5 illustrates the RD analysis for an experiment with a distance of 5 m and a water flow of 8.5 L/min. The same characteristic rain-induced pattern can be observed, as shown in the field at the WT installation (see discussion in the following). The pattern spreads between 0 and 5 m if we sprayed toward the radar, and between 5 and 10 m if we sprayed away from it. In the middle image, the pattern remains between 4.5 and 6 m, which is due to the width of the water jet. The pattern for $\theta = 90°$ is relatively weak, which can be explained by the larger distance between the metal frame and the radar, attenuation by the rain and by mirroring effects at the water front, where electromagnetic waves were reflected toward the ground. This means that the radar received a signal with a smaller amplitude. The same pattern also appears when the distance between the radar and the

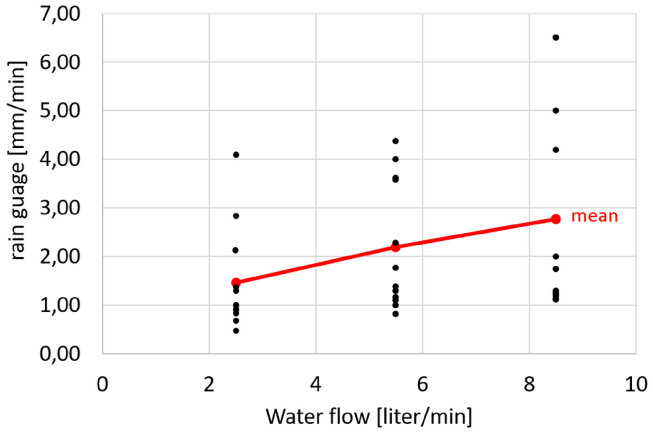

Fig. 4. Content of rain gauge determined after each measurement. In total, 36 measurements were recorded for three water flow levels (2.5, 5.5, and 8.5 L/min), three distances (5, 7, and 9 m), and three angular positions ($\theta = -90°$, $\theta = 0°$, and $\theta = 90°$). The horizontal axis represents the water flow and the vertical axis the mean of the content of both rain gauges. Due to the statistical properties of rain, the content of each gauge measurement was not the same for same angel θ. Therefore, the mean was considered in the simulation.

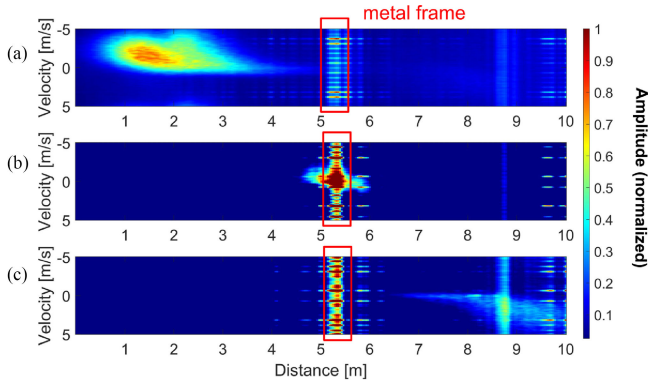

Fig. 5. RD analysis at a distance of 5 m with 8.5 L/min. In (a), the water was sprayed toward the radar ($\theta = -90°$). In (b), water was sprayed vertically down ($\theta = 0°$). In (c), the water was sprayed away from the radar ($\theta = 90°$).

metal frame (see Fig. 6) is increased. The only difference is that increasing the distance leads to a further reduction of amplitude in the RD map. The water flow has also a significant effect on the RD map. Fig. 7 reveals, on one hand, a larger distance between the metal frame and the water jet for an increasing water flow rate. On the other hand, the amplitude in the RD map changes accordingly. For a closer examination, the signal projections of the RD image were considered, which can be seen in Fig. 8. One can clearly distinguish the intensity by the amplitude of the signal.

A numerical study was then performed for validation of the experimental findings. Therefore, we calculated the number of rain drops using (4) with three different rain rates (see Table I). The rain rates depicted in Table I, which we measured in the laboratory experiments, are relatively high compared to natural rain. The laboratory experiment was limited by the minimum flow rate of the flow meter so that we were not able to reduce the rate to smaller values. Each rain-drop was modeled as a

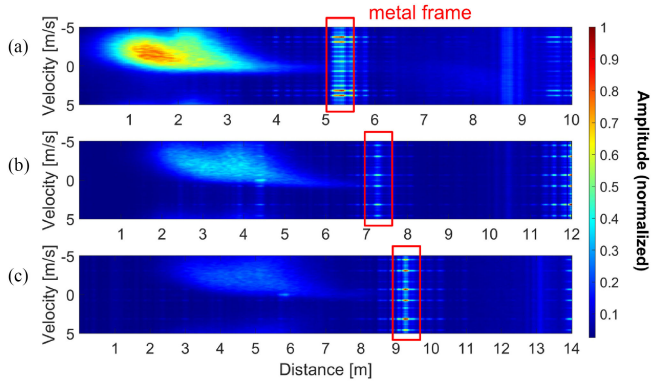

Fig. 6. RD analysis for different distances between radar and metal frame using $\theta = -90°$. The image depicted in (a) refers to a distance of 5 m, the image in (b) to 7 m, and the image in (c) to 9 m. The water intensity was adjusted to 8.5 L/min for all three cases.

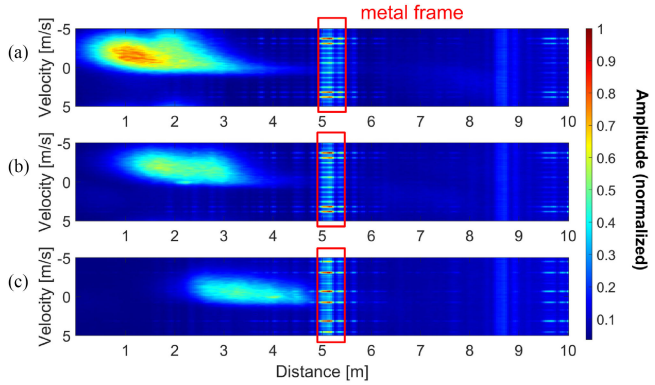

Fig. 7. RD analysis of various water flow intensities for $\theta = -90°$. In (a), the water intensity was adjusted to 8.5 L/min, in (b) to 5.5 L/min, and in (c) to 2.5 L/min.

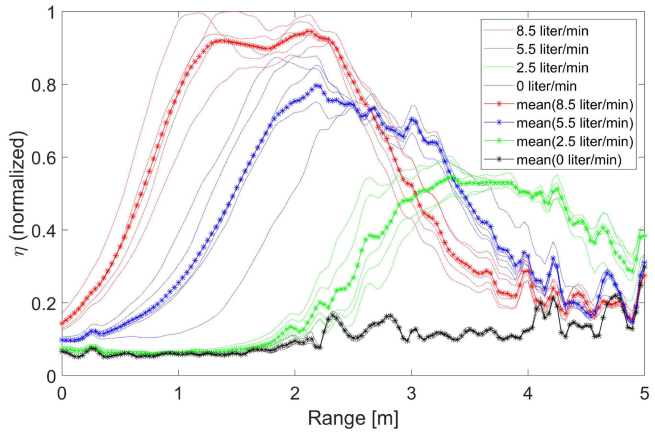

Fig. 8. Projections of the RD map onto the distance axis for the scenario shown in Fig. 7 with a distance between the radar and the metal frame of 5 m and $\theta = -90°$. The investigated flow rates as well as the case without rain can be clearly distinguished from each other.

TABLE I
NUMBER OF RAINDROPS PER CUBIC METER DEPENDING ON THE RAIN RATE (R) CALCULATED BY (4)

	R = 165 mm/h	R = 132 mm/h	R = 88 mm/h
N	5.696	5.436	4.994

The rain rate was derived from the rain gauge measurement depicted in Fig. 4.

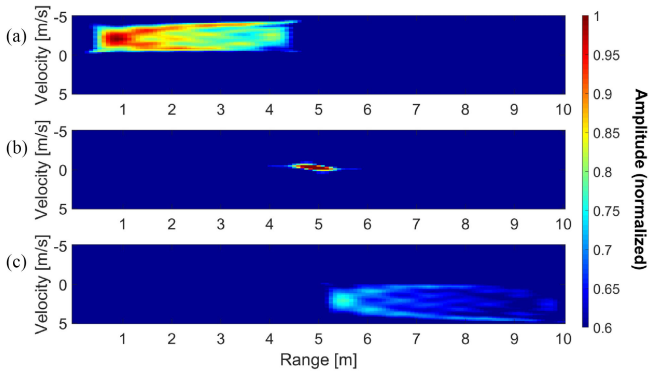

Fig. 9. Numerical result using the proposed FMCW signal model for modeling rain at a distance of 5 m and a rain rate of 165 mm/h. The simulation qualitatively models the laboratory measurements shown in Fig. 5. In (a), the water was sprayed toward the radar ($\theta = -90°$); in (b), water was sprayed vertically down ($\theta = 0°$; and in (c), the water was sprayed away from the radar ($\theta = 90°$).

Fig. 10. Illustration of the radar installation at a 2-MW WT at 95 m above the ground. Data were saved on a computer inside the WT tower.

point target and its reflectivity weighted by the Marshall–Palmer distribution. Fig. 9 shows the RD map obtained from simulations modeling the experiment with a distance of 5 m between the radar and the metal frame. The characteristic pattern for all three cases can be qualitatively identified for $\theta = -90°$, $\theta = 0°$, and $\theta = 90°$, respectively. In the simulation, natural weather conditions (e.g., weak wind during experiment) were neglected.

V. Field Installation at a 2-MW WT

Fig. 10 illustrates the radar system installed at the tower of a 2-MW WT about 95 m above the ground. A radar measurement and two videos have been recorded every 15 min. The first

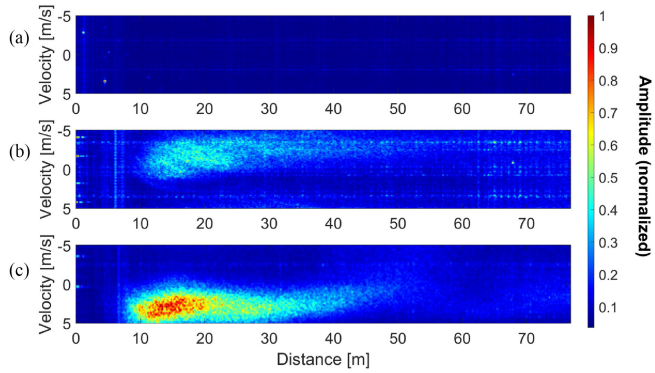

Fig. 11. RD map for different events at the WT. The picture depicted in (a) refers to a no-rain event. In (b), it rained moderately and in (c) heavily. The rain pattern known from laboratory measurements can be recognized here. Rain can be detected up to a distance of 80 m.

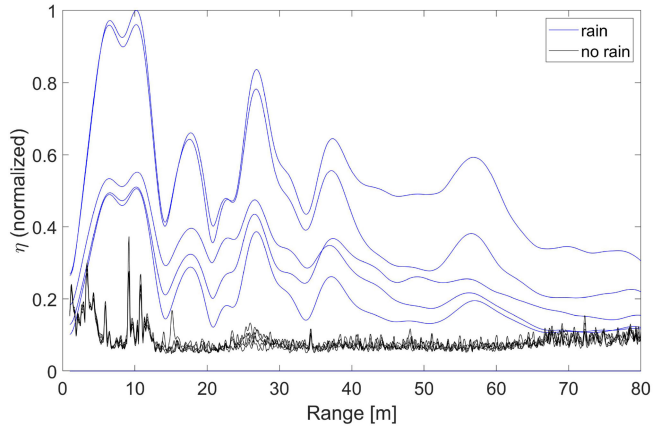

Fig. 12. Projection of the RD map of five data samples for rain and no rain measured at WT installation.

result is depicted in Fig. 11 and shows RD maps for no-rain, moderate-rain, and heavy-rain events, where the intensity was validated by the corresponding video. Compared to the laboratory results, we qualitatively obtain the same result. In a next step, we examined the WT data with the same RD method described before to find out if we can classify different rain conditions. Fig. 12 illustrates five projections of rain/no-rain states. The measurement conditions were then manually validated by the associated camera videos. Qualitatively, similar curves were observed as before so that the presence of rain can be easily discriminated from the rain absence condition.

Finally, we performed a classification of measurements for a total number of 2781 events, where 252 of them were rain events and 2569 were measured without rain. Therefore, the root mean square (rms) of the projected signal was determined. The result is shown in Fig. 13 with a clear difference between the two states. It must be mentioned that in the recorded data, only relatively few rain events were present. All of the recorded data used in this analysis were manually verified by video analysis. These results can serve as the basis for a more detailed classification of rainfall intensity in future work.

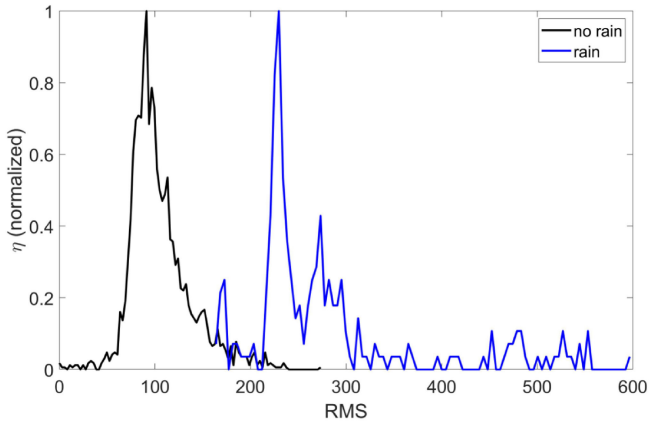

Fig. 13. Normalized histogram of rms of rain and no rain data from WT measurements. We only included video validated data here. In total, we evaluated 2781 events (252 rain events and 2569 no-rain events).

VI. Conclusion

This article successfully demonstrated the detection and classification of rain with a millimeter-wave radar system operating at 33.4–36.0 GHz. This functionality represents an additional feature in addition to structural inspection of the WT blades and detection of bats and birds in the WTs' near field. Numerical and experimental results were consistent in terms of characteristic patterns in the RD maps. This methodology provides real-time information of rain in the relevant flight zone of endangered animals with low-cost FMCW radar systems. In the future, a reliable detection of bats, birds, and precipitation can lead to an adaptive WT control strategy so that currently implemented shutdown algorithms leading to revenue losses can be overcome.

Acknowledgment

The authors are grateful to M. Dürr (Volta Windkraft GmbH, Ochsenfurt, Germany) for supporting the measurements at the wind turbine.

References

[1] *Global Wind Statistics 2017*, Brussels, Belgium, Global Wind Energy Council, 2018.
[2] R. Saidur, N. Rahim, M. Islam, and K. Solangi, "Environmental impact of wind energy," *Renew. Sustain. Energy Rev.*, vol. 15, no. 5, pp. 2423–2430, Jun. 2011.
[3] R. Brinkmann, O. Behr, I. Niermann, and M. Reich, Eds., *Entwicklung von Methoden zur Untersuchung und Reduktion des Kollisionsrisikos von Fledermäusen an Onshore-Windenergieanlagen: Ergebnisse eines Forschungsvorhabens* (ser. Umwelt und Raum. Schriftenreihe Institut für Umweltplanung). Göttingen, Germany: Cuvillier-Verl., (in German), 2011.
[4] J. Rydell, H. Engström, A. Hedenström, J. Larsen, J. Pettersson, and M. Green, *The Effect of Wind Power on Birds and Bats—A Synthesis*. Stockholm, Sweden: Swedish Environmental Protection Agency, 2012.
[5] C. C. Voigt, L. S. Lehnert, G. Petersons, F. Adorf, and L. Bach, "Wildlife and renewable energy: German politics cross migratory bats," *Eur. J. Wildlife Res.*, vol. 61, no. 2, pp. 213–219, Apr. 2015.
[6] L. Bulling, D. Sudhaus, D. Schnittker, E. Schuster, J. Biehl, and F. Tucci, *Vermeidungsmaßnahmen Bei Der Planung Und Genehmigung von Windenergieanlagen—Bundesweiter Katalog von Maßnahmen Zur Verhinderung Des Eintritts von Artenschutzrechtlichen Verbotstatbeständen Nach § 44 BNatSchG*. Berlin, Germany: Fachagentur Windenergie an Land (in German), 2015.
[7] *Leitfaden Artenschutz an Windenergieanlagen in Sachsen-Anhalt*, Ministerium für Umwelt Landwirtschaft und Energie des Landes Sachsen-Anhalt, (in German), Magdeburg, Germany, 2018.
[8] C. C. Voigt, K. Schneeberger, S. L. Voigt-Heucke, and D. Lewanzik, "Rain increases the energy cost of bat flight," *Biol. Lett.*, vol. 7, no. 5, pp. 793–795, Oct. 2011.
[9] D. R. Griffin, "The importance of atmospheric attenuation for the echolocation of bats," *Animal Behav.*, vol. 19, pp. 55–61, 1971.
[10] H. R. Goerlitz, "Weather conditions determine attenuation and speed of sound: Environmental limitations for monitoring and analyzing bat echolocation," *Ecol. Evol.*, vol. 8, no. 10, pp. 5090–5100, May 2018.
[11] M. Skolnik, *Radar Handbook*. New York, NY, USA: McGraw-Hill, 2008.
[12] F. Gekat *et al.*, "The-state-of-weather radar operations, networks and products," in *Weather Radar: Principles and Advanced Applications*, P. Meischner, Ed. Berlin, Germany: Springer, 2004, pp. 1–51.
[13] L. Lei, G. Zhang, R. J. Doviak, and S. Karimkashi, "Comparison of theoretical biases in estimating polarimetric properties of precipitation with weather radar using parabolic reflector, or planar and cylindrical arrays," *IEEE Trans. Geosci. Remote Sens.*, vol. 53, no. 8, pp. 4313–4327, Aug. 2015.
[14] A. Chandra, C. Zhang, P. Kollias, S. Matrosov, and W. Szyrmer, "Automated rain rate estimates using the Ka-band ARM zenith radar (KAZR)," *Atmos. Meas. Techn.*, vol. 8, no. 9, pp. 3685–3699, Sep. 2015.
[15] U. Görsdorf *et al.*, "A 35-GHz polarimetric doppler radar for long-term observations of cloud parameters—Description of system and data processing," *J. Atmos. Ocean. Technol.*, vol. 32, no. 4, pp. 675–690, Apr. 2015.
[16] J. Moll *et al.*, "Radar Imaging system for in-service wind turbine blades inspections: Initial results from a field installation at a 2MW wind turbine," *Prog. Electromagn. Res.*, vol. 162, pp. 51–60, 2018.
[17] J. Moll *et al.*, "Radar-based structural health monitoring of wind turbine blades: The case of damage detection," *Struct. Health Monit.*, vol. 17, no. 4, pp. 815–822, Jul. 2018.
[18] I. Cumming and J. Bennett, "Digital processing of seasat SAR data," in *Proc. IEEE Int. Conf. Acoust., Speech, Signal Process.*, Apr. 1979, vol. 4, pp. 710–718.
[19] J. C. Curlander and R. N. Mcdonough, *Synthetic Aperture Radar: Systems and Signal Processing*. Hoboken, NJ, USA: Wiley, 1991.
[20] A. Macaveiu, C. Nafornita, A. Isar, A. Campeanu, and I. Nafornita, "A method for building the range-Doppler map for multiple automotive radar targets," in *Proc. 11th Int. Symp. Electron. Telecommun.*, Nov. 2014, pp. 1–6.
[21] R. Bamler, "A comparison of range-Doppler and wavenumber domain SAR focusing algorithms," *IEEE Trans. Geosci. Remote Sens.*, vol. 30, no. 4, pp. 706–713, Jul. 1992.
[22] L. J. Rosen, *Encyclopedia of Physical Science*. New York, NY, USA: Infobase Publishing, 2009.
[23] *Digital Processing of Synthetic Aperture Radar Data: Algorithm and Implementation*. Norwood, MA, USA: Artech House, 2005.
[24] A. D. Byrd *et al.*, "A weather radar simulator for the evaluation of polarimetric phased array performance," *IEEE Trans. Geosci. Remote Sens.*, vol. 54, no. 7, pp. 4178–4189, Jul. 2016.
[25] E. Barcaroli, A. Lupidi, L. Facheris, F. Cuccoli, H. Chen, and C. V. Chandra, "A validation procedure for a polarimetric weather radar signal simulator," *IEEE Trans. Geosci. Remote Sens.*, vol. 57, no. 1, pp. 609–622, Jan. 2019.
[26] J. S. Marshall and W. M. K. Palmer, "The distribution of raindrops with size," *J. Meteorol.*, vol. 5, no. 4, pp. 165–166, 1948.
[27] B. J. Lipa and D. E. Barrick, *FMCW Signal Processing*. Sunnyvale, CA, USA: Mirage Systems, 1990.
[28] C. A. Balanis, *Advanced Engineering Electromagnetics*, 2nd ed. Hoboken, NJ, USA: Wiley, 2012.

Ashkan Taremi Zadeh received the B.Sc. and M.Sc. degrees in physics from Goethe University Frankfurt, Frankfurt, Germany, in 2016 and 2018, respectively, where he is currently working toward the Ph.D. degree in signal and data processing.

His research interests include signal processing, signal modeling, and radar imaging algorithms.

Moritz Mälzer received the B.Sc. and M.Sc. degrees in physics from Goethe University Frankfurt, Frankfurt, Germany, in 2016 and 2019, respectively, where he is currently working toward the Ph.D. degree in signal processing techniques.

His research interests include signal processing of ultrasonic guided waves.

Jonas Simon received the B.Sc. and M.Sc. degrees in computer science from Goethe University Frankfurt, Frankfurt, Germany, in 2016 and 2020, respectively.

He is currently a Research Assistant with Goethe University Frankfurt. His research interests include signal processing and imaging and the modeling and simulation of signal propagation.

Sebastian Beck received the Magister Artium degree in philosophy and history from Goethe University Frankfurt, Frankfurt, Germany, in 2012.

He is currently studying physics to become a physics and philosophy teacher with Goethe University Frankfurt. His current research interests include signal processing, computer science, and radar systems.

Jochen Moll received the Dipl.Ing. and Ph.D. degrees in mechanical engineering from the University of Siegen, Siegen, Germany, in 2007 and 2011, respectively.

He is currently a Postdoctoral Research Assistant with Goethe University Frankfurt, Frankfurt, Germany. His research interests include radar systems, signal processing, and imaging techniques. For more information, please visit: http://www.jochenmoll.de.

Viktor Krozer (Senior Member, IEEE) received the Dipl.-Ing. and Dr.-Ing. degrees in electrical engineering from Technical University Darmstadt, Darmstadt, Germany, in 1984 and 1991, respectively.

In 1991, he was a Senior Scientist with Technical University Darmstadt working on high-temperature microwave devices and circuits and submillimeter-wave electronics. From 1996 to 2002, he was a Professor with the Technical University of Chemnitz, Chemnitz, Germany. From 2002 to 2009, he was a Professor of Electromagnetic Systems with DTU Elektro, Technical University of Denmark, Kongens Lyngby, Denmark, where he was the Head of the Microwave Technology Group. Since 2009, he has been an endowed Oerlikon-Leibniz-Goethe Professor of Terahertz Photonics with Goethe University Frankfurt, Frankfurt, Germany, and heads the Goethe-Leibniz Terahertz Center. He is also with Ferdinand-Braun-Institut, Berlin, Germany, leading the THz Components and Systems Group. His research interests include terahertz electronics, monolithic microwave integrated circuits, nonlinear circuit analysis and design, device modeling, and remote sensing instrumentation.